Hanaa A. Muhammad [1]
Mohanad Q. Kareem [2]
Walla M. Mohammed [1]

[1] Department of Physics, College of Education for Pure Sciences, University of Tikrit, Tikrit, IRAQ
[2] Department of Physics, College of Science, University of Kirkuk, Kirkuk, IRAQ

Solvothermal Synthesis and Gas Sensing Properties of Nanostructured $La_6Sb_8S_{21}$ Composite Thin Films for Enhanced NO_2 Detection

In this work, Composite $La_6Sb_8S_{21}$ thin films were prepared and their structural, optical, and gas-sensing properties were studied. The nanostructured morphology and crystalline structure of the these films were revealed. As well, their optical characteristics such as absorption coefficients and energy band gaps have been determined. Electrical properties have been studied using I-V characteristic curves. Hall effect measurements were studied to determine the conductivity, resistivity, and charge carrier mobility. The gas-sensing performance of the prepared thin films was conducted at different operating temperatures in terms of sensitivity, response time, and recovery time. The results reveal that the composite $La_6Sb_8S_{21}$ thin films are ideal for gas sensing applications, particularly to NO_2 gas. Investigation has been extended to correlate the nanostructure, electronic properties and gas sensitivity, thus providing the broad outlook upon the new composite system.

***Keywords*:** Composites; Gas sensing; Thioglycolic acid; Solvothermal method
Received: 7 December 2024; **Revised:** 20 February; **Accepted:** 27 February 2025

1. Introduction

Currently, gas sensors are considered as one of the significant devices used in industries, industrial safety, environmental monitoring, and healthcare. The sensing materials have remained at the forefront of meticulous and exhaustive research in recent years. Among the various materials explored, metal oxide semiconductors have gained a significant attention due to their superlative sensing properties and easy manufacturing [1]. Lanthanum-based compounds have emerged as promising candidates for gas sensing applications due to their unique electronic properties and catalytic activity [2]. Lanthanum oxides, in particular, have shown remarkable sensing capabilities for a wide range of gases, including NO_2, CO, and H_2S [3]. Nevertheless, the pursuit of enhanced sensing performance has led researchers to investigate composite materials that combine the advantages of multiple components. The development of lanthanum antimony sulfur (La-Sb-S) composite nanomaterials denotes a novel approach in the field of gas sensing. These materials take superiority of the synergistic effects resulting from the catalytic properties of lanthanum, antimony's electronic features, and sulfur's capability to act as an modifier of the composite band structure [4]. Addition of sulfur into the LaSb matrix was documented to enhance substantially the sensor response towards some target gases, especially those with a strong electron-accepting nature such as NO_2 [5]. It has been observed that thin film technology is highly efficient in the fabrication of gas sensors in the quest for high surface-to-volume ratios, which is important to attain higher sensitivity and reduction of response times. Deposition techniques available to prepare composite La-Sb-S films are sputtering, chemical vapor deposition (CVD), and sol-gel. All these options have respective merits regarding film quality and scalability of the process [6,7]. Indeed, conventional applications in gas sensing being widely documented. The La-Sb-S nanocomposites currently demonstrated significant relevance to applications also in photocatalysis due to their tunable band gap and high surface area, which favor efficient light harvesting and charge separation [8,9], been explored, using the complex crystal structure as a means of securing low thermal conductivity with relatively good electrical functionality [10,11]. For gas sensor applications, from one perspective, some researches have suggested that La-Sb-S thin films feature superior qualities in terms of the detection of trace amounts of NO_2, a general air pollutant associated with combustion processes. High selectivity and low detection limits reached with these sensors render them adequate for environmental monitoring in urban areas and manufacturing environments [12,13]. Additionally, the prospects of operating at relatively low temperatures compared to conventional metal oxide sensors translate to potential energy savings in portable and continuous monitoring systems. The capability of the material to sense water vapor adsorption has been recently tested for humidity sensing as well, using La-Sb-S nanocomposites. This, in turn, renders the La-Sb-S-based sensors highly attractive for indoor air quality monitoring as a result of their dual functionality of detecting toxic gases and humidity levels [14,15]. In light of the ongoing development of this research, emphasis is placed on

optimization of composition and nanostructure in an effort to further the cause of their respective sensing capabilities. Integration of such advanced materials with miniaturized electronic platforms and wireless communication technologies opens up several avenues toward smart, networked sensing systems capable of performing real-time environmental monitoring on an unprecedented scale [16].

2. Expermintal methods

Thin films of $La_6Sb_8S_{21}$ were produced using solvothermal synthesis technique. The initial materials were 1.82g of $SbCl_3$, 2.22g of $LaCl_3$, 5mL of HCl, 1.0g of PVP, 1.38mL of Thioclic acid (TGA), 1.6g of thiourea, and 50ml of Dimethylformamide (DMF) solvent. The synthesis was conducted through dissolving metal chlorides in hydrochloric acid, accompanied by the addition of PVP, TGA, and thiourea. The blend was subsequently conveyed into a Teflon-lined high-pressure reactor and heated at 180 °C for 24 h. Later, after the precipitate cooled, it was collected, washed and dried at 60 °C for 12 h as shown in Fig. (1). The dried black compound was ground to ensure uniform particle size distribution and dispersed in ethanol. The suspension was then filtered and deposited on clean glass substrates using an insulin needle at 100 °C using the drop casting method. This process was repeated twice to achieve the desired thickness. The sample was then annealed at 300 °C for 3 min to improve crystallinity and remove organic residues. This step is very important when working to improve crystallinity and remove all residual organic bodies and thus improve the structural and functional properties of the film. The first step of substrate preparation prior to deposition has a strict prerequisite of cleaning the available substrate using a mixture of acetone and distilled water followed by rinsing with distilled water to remove any contaminants on the substrate and make a good surface for film deposition. The hot substrate deposition technique is used where 2 ml of the prepared solution is slowly added onto glass substrates preheated to 80 °C. This process enables consistent application of the material provided that scientists use it with the same degree of uniformity in their research. The second part of growth, distribution and film formation This integrated approach entails chemical convergence in action along with regulation in reaction conditions to generate high quality thin films with desired compositional and structural properties. A Bruker Advance D8 X-ray diffractometer was used to study the crystalline structures of the prepared films. A TESCAN MIRA3 FE-SEM instrument was used to examine the morphology and elemental compositions of the prepared films. A Shimadzu 100 UV-Visible spectrophotometer was used to determine the optical properties.

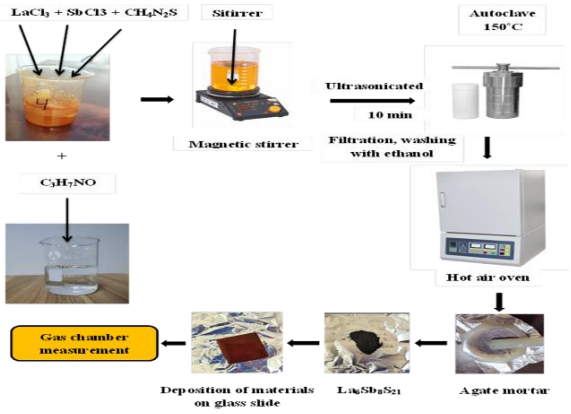

Fig. (1) Synthesis process of $La_6Sb_8S_{21}$ (TGA) thin films: from measurement to final product

The gas sensing properties were evaluated using a specialized NO_2 detection device. The apparatus comprised gas type: NO_2, concentration: 30 ppm, operating temperature range: from room temperature to 200 °C.

The test procedure included placing the sensor in the test chamber and making electrical connections. The chamber is evacuated to approximately 0.1 mbar. The flow rates of the carrier air and test gas are adjusted. The test gas is introduced into the chamber. The change in sensor resistance is measured in response to the gas. The sensor is allowed to return to baseline resistance. Measurements are repeated at different temperatures.

This comprehensive approach to synthesis, characterization, and gas sensing evaluation provides valuable insights into the properties and potential applications of $La_6Sb_8S_{21}$ thin films. The systematic diversity in composition and structure, when considered in combination with desired properties, allows the material properties to be tailored for specific sensing or other functional applications. The detailed gas sensing procedures ensure reliable and reproducible measurements, which is important in terms of evaluating the performance of the material as a gas sensor.

3. Results and Discussion

Figure (2) presents a comprehensive analysis of the morphology and composition of $La_6Sb_8S_{21}$ thin films by field-emission scanning electron microscopy (FE-SEM) at 35kx magnification. We observe an inhomogeneous surface topography, the film shows a mixture of smooth regions scattered with irregularly shaped particles and some visible cracks. This indicates a complex growth process during film deposition, which may entail island nucleation and coalescence.

Figure (3) provides a detailed view of the surface morphology at 70 kx magnification. We can distinguish the presence of nanoscale features including spherical particles and agglomerates. The different sizes of these

structures indicate a non-uniform growth process, which can be attributed to local differences in deposition conditions or thermal annealing post-deposition. In Fig. (4), at the highest magnification of 350 kx, individual nanoparticles become clearly visible and the size measurement of one of the particles indicates a diameter of 32.02 nm. This nanoscale dimension is important, as it is capable of profoundly influencing the digital, optical and catalytic properties of the material. The presence of nanostructures suggests potential applications in areas including sensing or catalysis, where high surface area-to-volume ratios are of high quality.

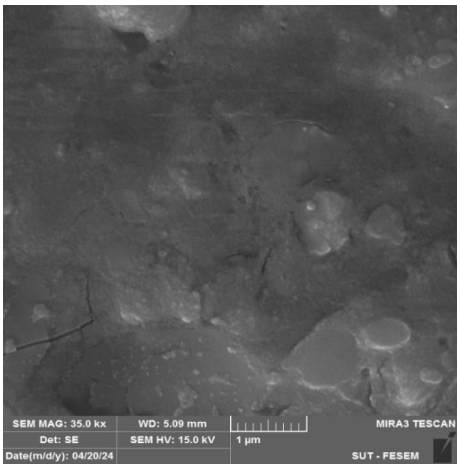

Fig. (2) FE-SEM image of $La_6Sb_8S_{21}$ composite thin films examined at magnification of 35.0 kx

Figure (5) represents the energy-dispersive x-ray (EDS) spectrum, providing crucial information about the elemental composition of the thin film. The spectrum confirms the presence of the expected elements: lanthanum (La), antimony (Sb), and sulfur (S), validating the successful synthesis of $La_6Sb_8S_{21}$. The relative peak intensities broadly correspond to the expected stoichiometry, with La showing the highest weight percentage (75.5%), followed by S (12.7%) and Sb (11.8%). The detection of gold (Au) peaks is likely as a result of the conductive coating applied to the sample for FE-SEM imaging, rather than being an intrinsic component of the film. The absence of significant impurity peaks suggests a high level of purity in the synthesized material.

The nanoscale structure observed in these FE-SEM images, combined with the confirmed composition from EDS, indicates the successful fabrication of $La_6Sb_8S_{21}$ nanocomposite thin films. This nanostructured morphology could potentially enhance the material's properties for various applications, such as improved gas sensing capabilities due to the high surface area, or unique optical properties arising from quantum confinement effects in the nanoscale regime. Further investigation of the film's electrical, optical, and functional properties would be valuable to fully characterize its potential for specific technological applications.

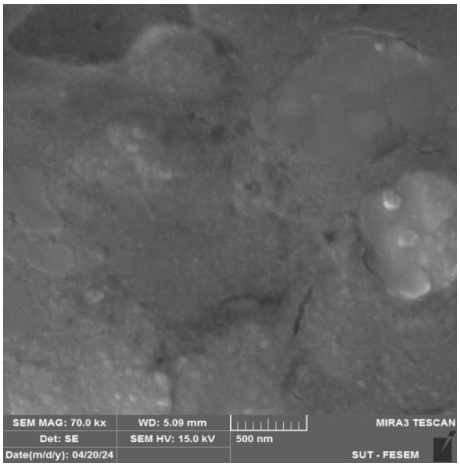

Fig. (3) FE-SEM image of $La_6Sb_8S_{21}$ composite thin films examined at magnification of 70.0 kx

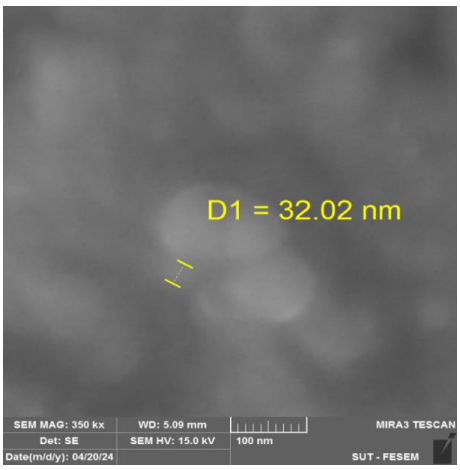

Fig. (4) FE-SEM image of $La_6Sb_8S_{21}$ composite thin films examined at magnification of 350 kx

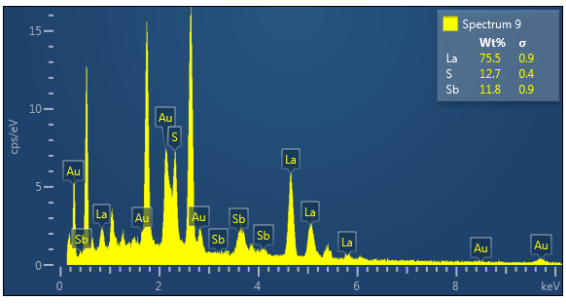

Fig. (5) EDX spectrum of the $La_6Sb_8S_{21}$ thin films prepared in this work

Error! Reference source not found. shows the X-ray diffraction (XRD) pattern of $La_6Sb_8S_{21}$ films. This pattern deliver essential data about the crystalline structure and phase composition. This analysis is based on the following elements: the experimental XRD sample of prepared $La_6Sb_8S_{21}$ films, pinnacle-green and the usual reference pattern from the JCPDS database, backside-purple. The XRD pattern of $La_6Sb_8S_{21}$ films

consists of a large number of well-described peaks, which suggests that these films are crystalline. The essential peaks are centered around 2θ of 23°, 25°, 27°, 32°, and 35°. These peaks are listed with their corresponding Miller indices (hkl), which include (320), (212), (420), (142), and (242), respectively. This could tend to suggest that the crystal shape is very complicated, as is common for ternary compounds similar to $La_6Sb_8S_{21}$. The experimental pattern agrees well with the reference JCPDS card 00-037-0583 with regard to top function and relative depth. This confirms the successful preparation of $La_6Sb_8S_{21}$ structure with high purity.

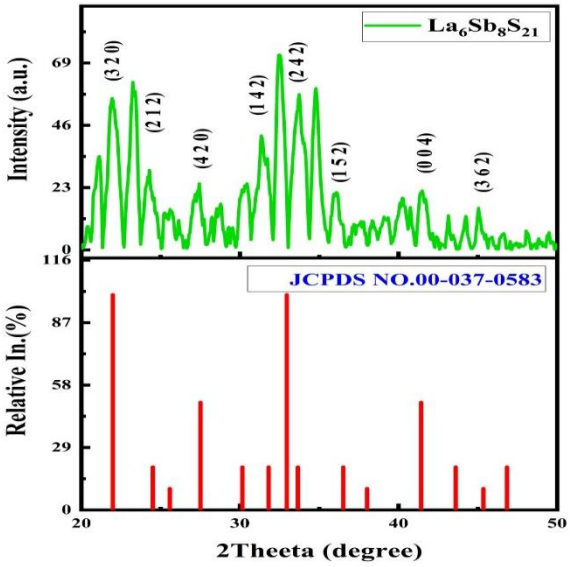

Fig. (6) XRD pattern of prepared $La_6Sb_8S_{21}$ thin films

The absence of additional peaks indicates that the sample is free from significant impurities or secondary phases, highlighting the effectiveness of the synthesis method in producing phase-pure $La_6Sb_8S_{21}$. The sharpness of the diffraction peaks in the experimental pattern suggests that the synthesized material consists of well-formed crystallites. The relatively high intensity of the peaks, particularly those at lower 2θ values, indicates that the crystallites are likely of good size, possibly in the nanometer to submicron range. This observation aligns with the nanocomposite nature of the films, as previously observed in the FE-SEM analysis. It's worthnoting that the experimental pattern shows some broadening of peaks compared to the idealized JCPDS reference. This broadening can be attributed to several factors, including the nanoscale crystallites (which introduces strain and size effects), potential lattice defects, and instrumental broadening. The Scherrer equation could be applied to estimate the average crystallite size from the full-width at half maximum (FWHM) of these peaks. The presence of all expected diffraction peaks with correct relative intensities suggests that the $La_6Sb_8S_{21}$ films do not exhibit significant preferred orientation. This isotropic crystallite distribution is advantageous for many applications, as it ensures consistent properties throughout the material. The structural properties are fundamental in determining the material's electronic, optical, and functional characteristics, making this XRD analysis a crucial step in characterizing the $La_6Sb_8S_{21}$ nanocomposite thin films for potential applications in areas such as optoelectronics, sensing, or catalysis. The most prominent peaks correspond to the (320), (212), (420), (142), (242), (152), (004), and (362) lattice planes, as identified in **Error! Reference source not found.**) provides a detailed comparison between the experimental and reference data. The lattice plane spacings (d-spacings) calculated from the XRD pattern closely match those from the JCPDS card, with minor variations likely due to strain or defects in the prepared films. The percentage contraction in d-spacing is generally small, ranging from -0.04316% to 0.04326%, suggesting good crystallinity of the sample. The FWHM values of the diffraction peaks offer insights into the crystallite size and lattice strain. Notably, the (420) plane exhibits the largest FWHM of 1.1808°, indicating smaller crystallite size or higher lattice strain along this direction. In contrast, the (004) and (362) planes show narrower peaks with FWHM values of 0.1476°, suggesting larger crystallites or less strain in these orientations. The relative intensities of the diffraction peaks are slightly different from the reference pattern and can be ascribed to preferred orientation effects in the prepared films. In fact, preferred orientation is one of the general phenomena for thin film samples, often arising during deposition or due to interaction with substrates. Considering that all the expected diffraction peaks were present and were in close agreement with the reference data, this confirms the formation of $La_6Sb_8S_{21}$ in a phase-pure form with good crystallinity. Although minor, the change in lattice parameters and peak intensities is instructive regarding the microstructure and growth characteristics of the prepared films, which correlates well with the optical and electronic properties for application purposes in optoelectronic devices or thermoelectric materials. The inter planar spacing (d) of the nanoparticle can be calculated using Bragg's law [17]

$$2dsin\theta_B = n\lambda \quad (1)$$

where θ_B represents Bragg's angle, n is an integer representing the diffraction order, diffraction is often ranked first, λ is the wavelength of incident x-rays

The average crystallite size (D_{avg}) is calculated using the Debye-Scherrer equation [18]

$$D_{avg} = \frac{k\lambda}{\beta cos\theta} \quad (2)$$

where k is a constant equal to 0.9, β is the FWHM, θ is the angle of maximum intensity calculated in degrees, and λ is the wavelength of x-rays

A comprehensive optical characterization of $La_6Sb_8S_{21}$ nanocomposite thin films offer valuable insights into their electronic structure and potential

applications in optoelectronic devices. **Error! Reference source not found.** illustrates the relationship between the absorption coefficient (α) and incident photon energy (hν). The absorption edge exhibits a sharp increase around 3.75 eV, indicating a well-defined band gap. This abrupt rise suggests good crystallinity and minimal defect states within the forbidden gap, which is consistent with the XRD analysis previously discussed. **Error! Reference source not found.** depicts the Tauc plot for direct allowed transitions, where $(\alpha h\nu)^2$ is plotted versus hν. The linear extrapolation of the absorption edge yields a direct bandgap of 4.1 eV. This relatively wide bandgap places $La_6Sb_8S_{21}$ in the category of wide-bandgap semiconductors, suggesting potential applications in UV optoelectronics or as a transparent conducting material. Interestingly, **Error! Reference source not found.** reveals an indirect allowed transition with a bandgap of 3.79 eV. The presence of both direct and indirect transitions indicates a complex band structure, which is not uncommon in ternary compounds. The smaller indirect bandgap could facilitate enhanced light absorption in the near-UV region, potentially improving the material's photoresponse in certain applications.

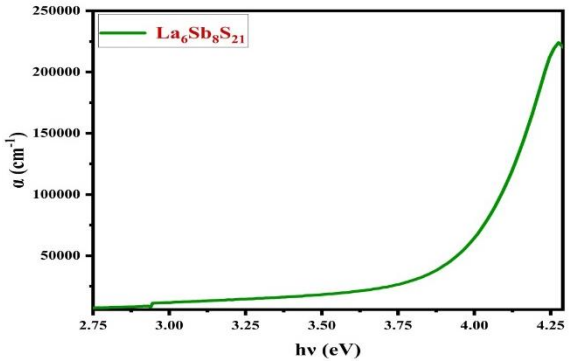

Fig. (7) Relationship of absorption coefficient (α) with photon energy (hν) for $La_6Sb_8S_{21}$ nanocomposite thin films

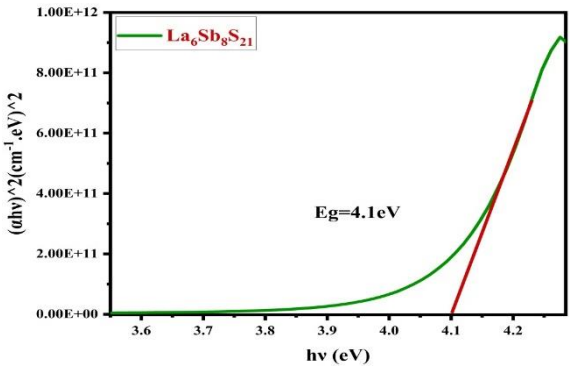

Fig. (8) determination of energy gap for the direct allowed transition in $La_6Sb_8S_{21}$ nanocomposite thin films

The excitation spectrum shown in **Error! Reference source not found.** provides further insight into the optical properties of $La_6Sb_8S_{21}$ samples. It features an excitation peak at 626.95 nm, corresponding to the energy of 1.97 eV. Given this, the feature likely represents a sub-bandgap transition, such as one arising from defect states or impurities in the crystal lattice. Such transitions may be useful in relation to photocatalytic applications or in enhancing the luminescence properties of the material. Such coexistence of wide direct and indirect bandgaps, even further assisted by sub-bandgap excitation, holds very promising prospects in tailoring the optical response of nanocomposite $La_6Sb_8S_{21}$ thin films.

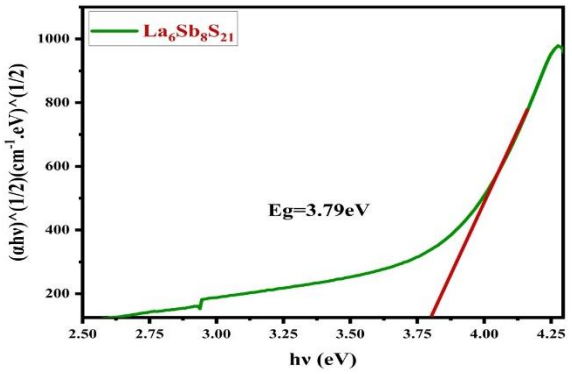

Fig. (9) determination of energy gap for the indirect allowed transition in $La_6Sb_8S_{21}$ nanocomposite thin films

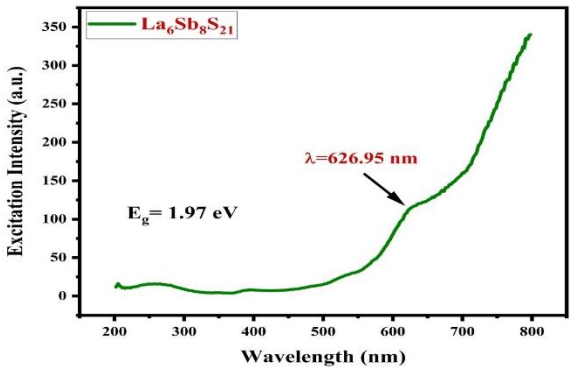

Fig. (10) Excitation intensity as a function of wavelength for nanocomposite $La_6Sb_8S_{21}$ thin films

These features are used within a multi-junction solar cell approach where two absorption bands are taken in order to increase higher overall efficiency. Besides, the wide bandgap nature of the material promises use as a transparent conducting oxide, especially upon the implementation of appropriate doping strategies that can enhance its electrical conductivity. The optical data also afford important information for the band structure calculations and theoretical modeling of $La_6Sb_8S_{21}$. These values of bandgap and transition energies constitute very important benchmarks that help in refining theoretical predictions and hence in understanding fundamental electronic properties of this complex ternary compound.

The current-voltage (I-V) characteristics of $La_6Sb_8S_{21}$ films in dark and under illumination afford

valuable information concerning electrical and photoconductive properties of the material. **Error! Reference source not found.**(11) presents the complete I-V curve for the forward and reverse bias regions. In dark conditions (red curve), the material exhibits near-symmetric behavior with minimal current flow in both directions, indicating a high resistance state.

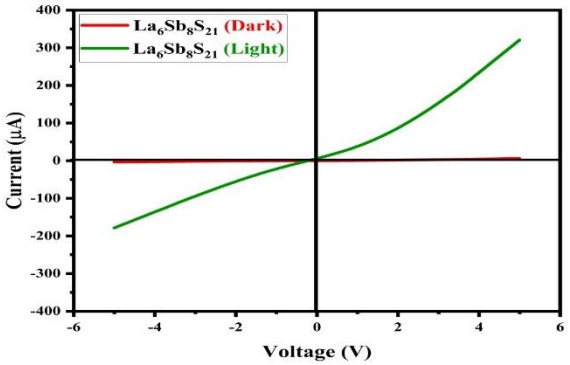

Fig. (11) Current-voltage characteristics (forward and reverse biasing) for $La_6Sb_8S_{21}$ thin films

This suggests that $La_6Sb_8S_{21}$ behaves as a wide-bandgap semiconductor or insulator in its intrinsic state, consistent with the optical bandgap measurements discussed earlier. Under illumination (green curve), a dramatic change in the I-V characteristics is observed. The curve becomes highly asymmetric, with a significant increase in current flow, particularly in the forward bias region. This photo response demonstrates the material's potential for optoelectronic applications, such as photodetectors or photovoltaic devices. The pronounced difference between dark and light conditions indicates a high photosensitivity, which can be attributed to the generation of electron-hole pairs upon light absorption. Asymmetry in the illuminated I-V curve indicates the presence of a photovoltaic junction, either at the interface between the $La_6Sb_8S_{21}$ film and substrate, or across the grain boundaries in the polycrystalline structure. For clarity, **Error! Reference source not found.** shows an enlargement of the forward bias region. Further evidence of this is given by the quite low value of the dark current (red curve) for all voltages, which provides the high resistivity of the material in the dark. In contrast, the illuminated current, shown in green, reveals a nonlinear dependence with respect to the applied voltage representative of a photoconductive or photovoltaic response. The shape of the illuminated I-V curve in the forward bias region informs about charge transport mechanisms. Nonlinear behavior points to SCLC or to trap-assisted conduction processes. This phenomenon is not exceptional in polycrystalline or nanostructured materials, as grain boundaries and defect states can usually play an influential role in carrier dynamics. A large discrepancy between dark and light current at a high voltage also signifies high photoconductive gain. This property is particularly helpful in sensitive photodetectors for the detection of low-intensity light signals. The low voltage onset of photocurrent in the forward bias region evidences a small turn-on voltage of photoconductivity, which is useful in low-power optoelectronic devices due to efficient charge separation and collection occurring in the material. I-V characteristics can be used as guidelines to optimize $La_6Sb_8S_{21}$ films for specific applications. For instance, the high dark resistance and strong photo response highlight the promise the material holds for high-sensitivity photodetectors with low dark current noise. Besides, the I-V curve asymmetry in the presence of light indicates that the material could prove useful for photovoltaic applications, too, though quantum efficiency and carrier lifetime would also need to be studied in order to find out true suitability for fabricating solar cells. These current-voltage characteristics investigated on $La_6Sb_8S_{21}$ films manifest materials with very interesting optoelectronic properties, having both high resistance in the dark and strong photosensitivity. These properties, combined with the wide bandgap nature of the material, open vistas of possibilities for numerous applications in UV-sensitive devices, transparent electronics, and potentially novel photovoltaic structures.

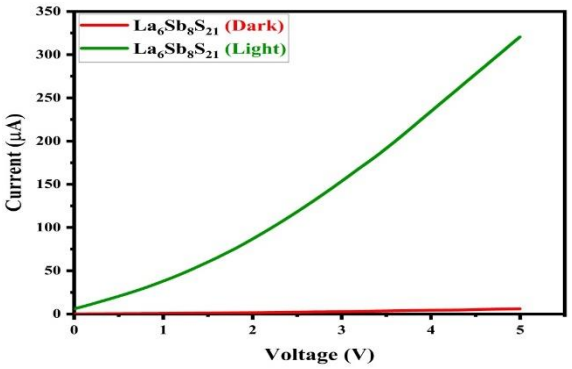

Fig. (12) Current-voltage characteristics (forward bias only) for $La_6Sb_8S_{21}$ thin films

Table (3) and **Error! Reference source not found.**) provide crucial electrical and thermoelectric data for $La_6Sb_8S_{21}$ films, offering insights into its transport properties and potential applications in electronic devices. The Hall Effect measurements in Table (3) reveal the material's complex electronic behavior.

The Hall effect principle relies on the Lorentz force experienced by charge carriers in a magnetic field, allowing determination of carrier type, concentration, and mobility. The equation for the Hall coefficient (R_H) is [19]:

$$R_H = V_H / (JB) \quad (3)$$

where V_H is the Hall voltage, J is the current density, and B is the magnetic field strength

The wide range of Hall motility values observed from -8.10×10^4 to 2.40×10^5 $cm^2/V.s$ suggests a strong dependence on measurement conditions or sample variations. The negative mobility values indicate n-type conductivity, likely resulting from intrinsic defects or unintentional doping. The conductivity (σ) and resistivity (ρ) values span several orders of magnitude, reflecting the material's sensitivity to external factors. The relationship between these parameters and carrier concentration (n) and mobility (μ) is given by [20]:

$$\sigma = 1/\rho = ne\mu \quad (4)$$

The temperature dependence of conductivity (table 3) provides information on the material's activation energy and conduction mechanisms. The plot of $\ln(\sigma_{dc})$ versus 1000/T allows extraction of the activation energy (E_a) using the Arrhenius equation [21]:

$$\sigma = \sigma_0 \exp(-E_a/kT) \quad (5)$$

where σ_0 is a pre-exponential factor, k is the Boltzmann constant, and T is absolute temperature

Table (1) Data of plot of $\ln(\sigma_{dc})$ versus (1000/T) for $La_6Sb_8S_{21}$

Temperature (K)	Conductivity (σ)	1000/T	Ln(σ)
301	0.000000252	3.2226	-0.15.1938
301	0.00135	3.2226	-6.6076
301	0.00495	3.2226	-5.3083

The non-linear nature of this plot suggests multiple conduction mechanisms or temperature-dependent activation energies. At lower temperatures, extrinsic conduction likely dominates, while intrinsic conduction becomes more prominent at higher temperatures. These results highlight the complex electronic structure of $La_6Sb_8S_{21}$. The large bandgap nature was pointed out by the optical measurements and was in good agreement with the high resistivity observed in part of the electrical measurements. However, the large dispersion in the electrical properties evidences a strong influence of either defects, grain boundaries, or surface states on the charge-transport mechanism. Thus, with high mobility combined with tunable conductivity, $La_6Sb_8S_{21}$ becomes an attractive candidate for versatile electronic applications. That it is sensitive to external conditions promises further applications as sensors or devices of adaptive electronics. Besides, the possibility of tailoring its electrical properties either by doping or by defect engineering opens ways for tuning this material for specific applications in either optoelectronics or thermoelectrics. With this, it should now be clear that the electrical characterization of $La_6Sb_8S_{21}$ has brought out a material with rich and complex electronic behavior. Deep searches on the nature of the defects, carrier scattering mechanisms, and band structure would be increasingly important in further optimizing the material for practical application and in understanding some of its basic physical properties.

The sensing properties based on the resistance in detail presents the gas sensing properties of $La_6Sb_8S_{21}$ films at different temperatures and hence an idea of their application possibility in chemical sensors. **Error! Reference source not found.**) shows the response at room temperature. After the gas exposure the resistance increased quickly up to a peak value of approximately 1.75 MΩ. This sharp rise indicates a strong interaction between the target gas molecules and the $La_6Sb_8S_{21}$ surface. The subsequent decrease in resistance during continued gas exposure suggests a dynamic equilibrium between gas adsorption and desorption processes. Upon gas removal, the resistance gradually returns to its baseline, demonstrating the reversibility of the sensing mechanism.

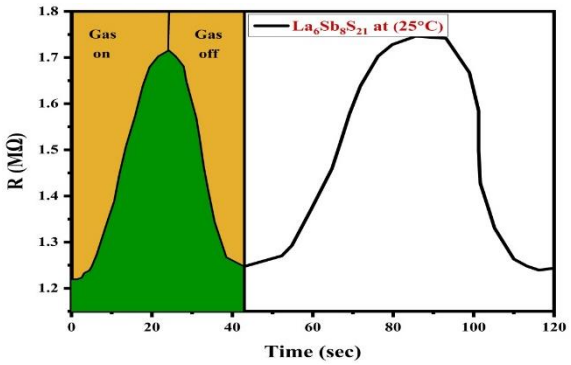

Fig. (13) Variations in resistance with time at 25°C for $La_6Sb_8S_{21}$ thin films

In **Error! Reference source not found.**at 100°C, the overall resistance decreases compared to room temperature, which is consistent with the semiconducting nature of $La_6Sb_8S_{21}$. The response pattern remains similar, but with a reduced magnitude, peaking at about 1.5 MΩ. This temperature-dependent behavior likely reflects changes in the gas-surface interaction dynamics and charge carrier concentration within the material.

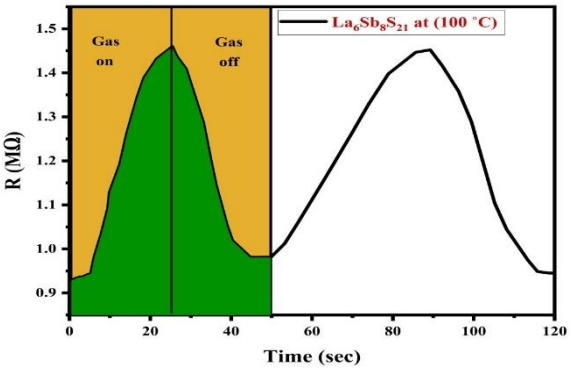

Fig. (14) Variations in resistance with time at 100°C for $La_6Sb_8S_{21}$ thin films

Further heating to 200°C, **Error! Reference source not found.** (15) results in a more pronounced decrease in baseline resistance, now below 1 MΩ.

Interestingly, the sensing response exhibits a markedly different profile. The initial resistance increase upon gas exposure is followed by a more rapid return to baseline, even while the gas is still present. This behavior suggests enhanced desorption kinetics or possibly a change in the dominant sensing mechanism at elevated temperatures.

Temperature-dependencies of the sensing characteristics of $La_6Sb_8S_{21}$ films gives evidence for the complex interplay between the different factors. The strong room temperature response suggests that surface reactivity is high, most probably caused by the appearance of active sites for gas adsorption. The resistance changes reflect the donation or abstraction of electrons between the adsorbed gas molecules and the $La_6Sb_8S_{21}$ surface, determining its conductivity. With the increase in temperature, the mobility of the gas molecules might increase, which, in turn, could be responsible for the faster response and recovery times for both adsorption and desorption. Temperature can increase defect concentration or change ionization state and may affect intrinsic carrier concentration, consequently changing the gas-sensing behavior of a material. It has not explicitly been observed in this work; still, subtle structural changes at an elevated temperature cannot be absolutely excluded for $La_6Sb_8S_{21}$ and might thus impact its sensing behaviour. These results present $La_6Sb_8S_{21}$ films as promising candidates for their gas-sensing performance over a wide temperature range. Its high sensitivity at room temperature will be very beneficial for low-power sensor design.The distinct response patterns at different temperatures suggest the possibility of selective gas detection through temperature modulation.

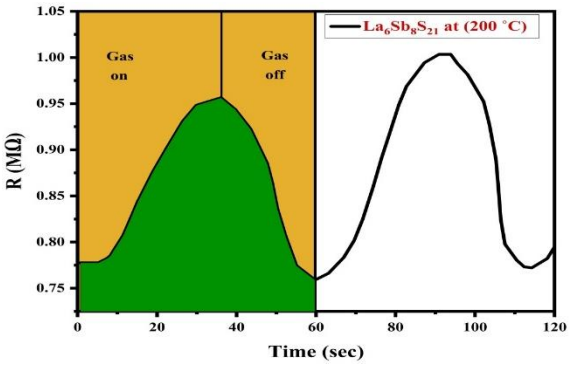

Fig. (15) Variations in resistance with time at 200°C for $La_6Sb_8S_{21}$ thin films

The data presented in **Error! Reference source not found.** and **Error! Reference source not found.**) illustrate the performance characteristics of $La_6Sb_8S_{21}$ thin film sensors when exposed to 30 ppm NO_2 at varying operating temperatures. The sensitivity of the sensor, depicted in **Error! Reference source not found.**), exhibits a non-linear relationship with temperature. It peaks at 100°C with a value of 53.19%, significantly higher than the sensitivities observed at room temperature (38.78%) and 200°C (21.79%). This bell-shaped curve suggests an optimal temperature range for sensor operation, likely due to the interplay between gas adsorption kinetics and charge carrier mobility within the sensing material. Response and recovery times, crucial parameters for real-time gas sensing applications, demonstrate interesting trends.

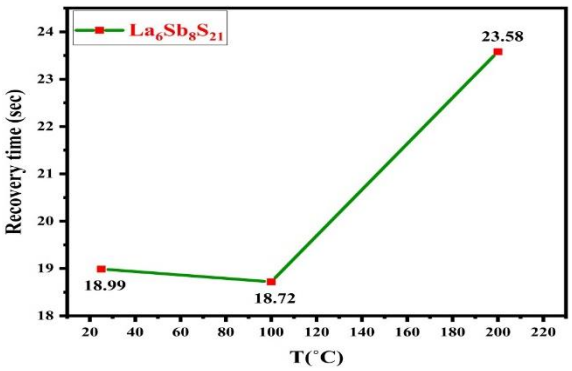

Fig. (16) Variations in recovery time with operating temperatures

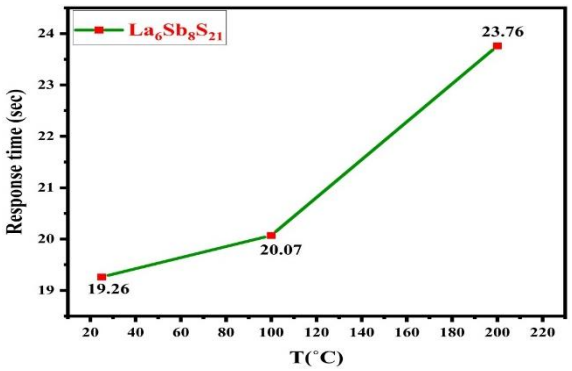

Fig. (17) Variations in response time with operating temperatures

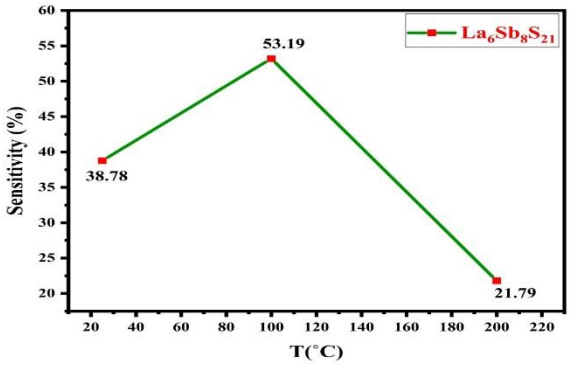

Fig. (18) Variations in sensitivity with operating temperatures

The response time (**Error! Reference source not found.**) increases gradually with temperature, from 19.26 s at room temperature to 23.76 s at 200°C. This slower response at higher temperatures may be attributed to changes in the sensor's surface chemistry or charge transfer mechanisms. Conversely, the recovery time in **Error! Reference source not found.**) remains relatively stable between room temperature

and 100°C (18.99 s and 18.72 s, respectively, before increasing markedly to 23.58 s at 200°C. This behavior could be related to the desorption kinetics of NO_2 molecules from the sensor surface, which may become more complex at elevated temperatures. The interrelation between sensitivity, response time, and recovery time presents an engineering trade-off. Although the maximum sensitivity occurs at 100°C, this temperature does not correspond to either the fastest response or recovery times. Thus, the optimal operating temperature of sensor devices developed around $La_6Sb_8S_{21}$ would depend on the exact requirements of the particular application concerning sensitivity versus response dynamics. Results presented herein provide insight into the temperature-dependent sensing mechanism of $La_6Sb_8S_{21}$ thin films. Such trends could be interpreted as due to several phenomena: changes in surface adsorption sites, in band structure, or in charge carrier concentration and mobility with temperature. Further investigation of the underlying physical and chemical processes would allow a precise identification of mechanisms involved in such performance characteristics and might be of value in the design of more efficient gas-sensing materials.

4. Conclusion

Comprehensive studies on $La_6Sb_8S_{21}$ thin films have revealed promising properties related to gas sensing performance. The nanostructure and the crystal structure contribute to the increased surface area and reactivity of the material. Optical studies reveal the adjustable band gap characteristics, which is important for improving the sensor performance. Electrical measurements provide insights into the charge transport mechanisms within the compound. Gas sensing experiments performed at different temperatures highlight the ability of this material to detect NO_2 with good sensitivity and reasonable response and recovery times. The temperature dependence of the observed sensing behavior indicates an ideal operating range in practical applications. The structural, optical and electrical properties of the material, as well as the gas sensing performance, provide a strong basis for further improvement of $La_6Sb_8S_{21}$-based sensors.

References

[1] B. Saruhan et al., "Influences of semiconductor metal oxide properties on gas sensing characteristics", *Front. Sens.*, 2 (2021) 657931.

[2] M.K. Tiwari et al., "Advancements in lanthanide-based perovskite oxide semiconductors for gas sensing applications: a focus on doping effects and development", *Anal. Meth.*, 43 (2023) 5754-5787.

[3] K. Shingange, "The exploration of lanthanum based complexes oxides: preparation, characterization and gas sensing properties", PhD thesis, University of The Free State (2019).

[4] M.B. Hanif et al., "Recent advancements, doping strategies and the future perspective of perovskite-based solid oxide fuel cells for energy conversion", *Chem. Eng. J.*, 428 (2022) 132603.

[5] K. Luo et al., "Advances in carbon nanotube-based gas sensors: Exploring the path to the future", *Coord. Chem. Rev.*, 518 (2024) 216049.

[6] M.Q. Kareem et al., "Synthesis of Tetrahedrite Zincian Nanocomposites via solvothermal process at low temperature", *Ceram. Int.*, 50 (2024) 40005-40013.

[7] D.Q. Tan, "Review of polymer-based nanodielectric exploration and film scale-up for advanced capacitors", *Adv. Funct. Mater.*, 30 (2020) 1808567.

[8] T. Vijayaraghavan and A. Ashok, "Oxide based Nanocomposites for Photocatalytic Applications", in: Applied Nanocomposites, CRC Press (2022), pp. 55–89.

[9] A. Kubacka, M. Fernandez-Garcia and G. Colon, "Advanced nanoarchitectures for solar photocatalytic applications", *Chem. Rev.*, 112 (2012) 1555-1614.

[10] K. Yuan et al., "Engineering the thermal conductivity of functional phase-change materials for heat energy conversion, storage, and utilization", *Adv. Funct. Mater.*, 30 (2020) 1904228.

[11] H. Chen et al., "Thermal conductivity of polymer-based composites: Fundamentals and applications", *Prog. Polym. Sci.*, 59 (2016) 41–85.

[12] C. Dincer et al., "Disposable sensors in diagnostics, food, and environmental monitoring", *Adv. Mater.*, 31 (2019) 1806739.

[13] W. Bourgeois et al., "The use of sensor arrays for environmental monitoring: interests and limitations", *J. Environ. Monit.*, 5 (2003) 852–860.

[14] M. Ródenas García et al., "Review of low-cost sensors for indoor air quality: Features and applications", *Appl. Spectrosc. Rev.*, 57 (2022) 747–779.

[15] H. Zhang and R. Srinivasan, "A systematic review of air quality sensors, guidelines, and measurement studies for indoor air quality management", *Sustainability*, 12 (2020) 9045.

[16] F.J. Tovar-Lopez, "Recent progress in micro-and nanotechnology-enabled sensors for biomedical and environmental challenges", *Sensors*, 23 (2023) 5406.

[17] T. Egami and S.J.L. Billinge, **"Underneath the Bragg peaks: structural analysis of complex materials"**, Elsevier (2003).

[18] K.D. Karlin (ed.), **"Progress in Inorganic Chemistry"**, vol. 59, John Wiley & Sons (NJ, 2014).

[19] P. Holister et al., Nanoparticles: Technology White Paper No.3, Científica, 11. www.cientifica.com (2003).
[20] D. Yang, "Applications of Laser Ablation - Thin Film Deposition, Nanomaterial Synthesis and Surface Modification", IntechOpen (2016).
[21] M.V. Reddy et al., "Solid State Ionics: Ionics for Sustainable World", *Proc. 13th Asian Conf.*, 265 (2012).

Table (2) XRD analysis with experimental XRD data, standard values for $La_6Sb_8S_{21}$ and FWHM values

2θ (deg)	FWHM (deg)	d_{XRD} (Å)	d_{JCPDS} (Å)	% Contraction in d	(hkl)	Phase	Card No.
21.984	0.2460	3.99674	4.04000	0.04326	(320)	Orthorhombic	00-037-0583
24.503	0.5904	3.67316	3.63000	-0.04316	(212)	Orthorhombic	
27.507	1.1808	3.23258	3.24000	0.00742	(420)	Orthorhombic	
31.809	0.2460	2.81740	2.81100	-0.0064	(142)	Orthorhombic	
33.653	0.2460	2.66680	2.66100	-0.0058	(242)	Orthorhombic	
36.511	0.3936	2.45751	2.45900	0.00149	(152)	Orthorhombic	
41.424	0.1476	2.15412	2.17800	0.02388	(004)	Orthorhombic	
45.354	0.1476	1.99641	1.99800	0.00159	(362)	Orthorhombic	

Table (3) Values of the temperature, conductivity, resistivity, mobility, current and Hall coefficient for $La_6Sb_8S_{21}$

Temperature (SV)	Temperature (PV)	Current (A)	Resistivity (Ω.cm)	Conductivity $(\Omega.cm)^{-1}$	Mobility $(cm^2/V.s)$	Avg. Hall Coefficient $(m^3/A.s)$
301	301	2.00E-08	3.97E+06	2.52E-07	6.03E-02	2.40E+05
301	301	2.00E-08	7.42E+02	1.35E-03	1.09E+02	-8.10E+04
301	301	2.00E-08	2.02E+02	4.95E-03	2.59E+02	-5.23E+04

Table (4) The sensitivity, response, and recovery times of the thin film sensors upon exposure to the targeting gas at different operating temperatures

Sample	Gas type	T (°C)	S (%)	Response time t_s (s)	Recovery time t_c (s)
$La_6Sb_6S_{21}$	NO_2 (30ppm)	RT	38.78	19.26	18.99
		100	53.19	20.07	18.72
		200	21.79	23.76	23.58

